J. Fluid Mech. (1970), *vol.* 45, *part* 1, *pp.* 65–90
Printed in Great Britain

Measurements of the wave-number/phase velocity spectrum of wall pressure beneath a turbulent boundary layer

By J. A. B. WILLS
Aerodynamics Division, National Physical Laboratory, Teddington

(Received 22 October 1968 and in revised form 27 July 1970)

Measurements are presented of the wave-number/frequency and wave-number/phase velocity spectrum of wall pressure for a two-dimensional turbulent boundary layer in zero pressure gradient, obtained from a Fourier transform of experimental filtered spatial correlations. This method allows the results to be corrected for acoustic disturbances in the wind tunnel, and for finite transducer size. An empirical form for the pressure field is proposed, based on the measurements, and is used to predict a frequency spectrum correction for transducer size which agrees well with measured values.

1. Introduction

The problem of the fluctuating pressure field on the wall beneath a turbulent boundary layer or a pipe flow has excited considerable interest since the advent of pressure transducers small and sensitive enough to give detailed measurements in low speed flows. The interest arises mainly because the pressure field may produce vibrations of the wall, possibly resulting in the generation or transmission of noise in the case of an aircraft, or even causing fatigue of the metal. The study of the pressure field is also important in its own right for the information it can yield on the structure of the turbulence in the boundary layer.

Because the mean shear and turbulence intensity within the boundary layer are high, the analysis carried out by Lin (1952) leads us to expect that Taylor's hypothesis will not hold for the pressure fluctuations on the wall, i.e. there is no single velocity at which all the elementary pressure disturbances travel. For this reason, most investigators (cf. Bull & Willis 1961; Corcos 1962; Willmarth & Wooldridge 1962) have measured the longitudinal space-time correlation of the pressure fluctuation,

$$R_{pp}(\xi,\tau) = \overline{p(x,t).p(x+\xi,t+\tau)},$$

using the techniques developed originally by Favre, Gaviglio & Dumas (1957) for the correlations of velocity fluctuations in turbulent flows. These data have been used to calculate effective convection velocities for the turbulent motion, and to estimate average life-times of eddies of various scales. For example, Willmarth & Wooldridge (1962) presented their data as a contour plot of the correlation as a function of space and time separation, as in figure 1. The convection velocity was defined as the slope of a line through the peaks of the contours, shown as a dotted

line in figure 1. In the experiment of Willmarth & Wooldridge, this line was found to be curved, so that the convection velocity obtained was a function of the space or time separation between the transducers, varying from $0{\cdot}56\,U_\infty$ for zero separation to $0{\cdot}83\,U_\infty$ for large separation.

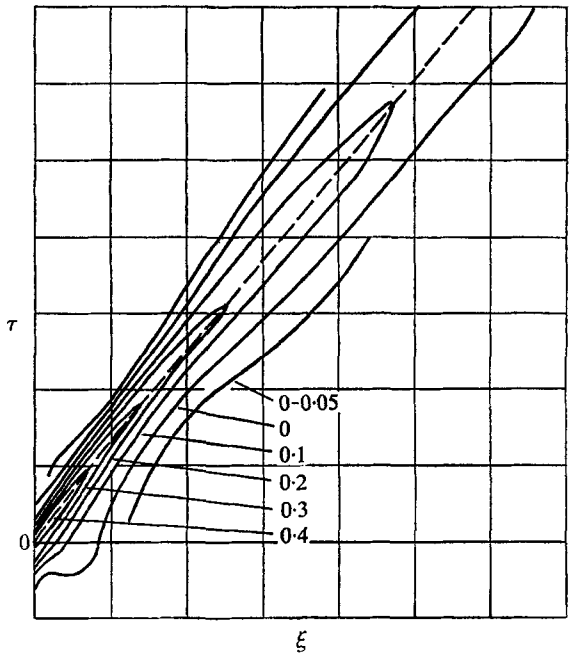

FIGURE 1. Diagrammatic representation of the $R_{pp}(\xi, \tau)$ contours of Willmarth & Wooldridge.

For the near-homogeneous flow investigated by Willmarth & Wooldridge, this variation in convection velocity must be attributed to the fact that, for small separations, the correlation is dominated by the small-scale eddies close to the wall, travelling relatively slowly, while for large separations these eddies will have decayed, leaving the faster-moving large-scale eddies to determine the convection velocity.

For some applications of the results, it is desirable to have a more definite relation between convection velocity and eddy size, and Willmarth & Wooldridge attempted to obtain this relation by measuring the convection velocity in two filtered bands of low and high frequency. However, for a situation where the effective convection velocity varies with wave-number, frequency filtering is not equivalent to isolating a particular wave-number, so that Willmarth & Wooldridge again found a convection velocity that increased with increasing transducer separation. Similar results have been found by Favre, Gaviglio & Fohr (1964) for velocity fluctuations in a boundary layer, using filters of much narrower bandwidth (Willmarth & Wooldridge attributed the variation of their filtered convection velocity with separation to an insufficiently narrow bandwidth).

The difficulty arises because a frequency filter cannot distinguish between eddies of large wavelength moving quickly and eddies of small wavelength

moving slowly. The turbulent pressure field can be considered as a distribution of energy over a range of wave-numbers, each wave-number having a distribution of phase velocities $c \equiv \omega/k_1$, and a frequency filter picks out those parts of the field for which the product of wave-number and phase velocity is a constant. In an earlier paper (Wills 1964), the author outlined an alternative approach to the presentation of data on turbulent fluctuations, involving the measurement of the complete wave-number/phase velocity spectrum. An experimental method was described which had several advantages, particularly for the measurement of pressure in the presence of the spurious sound fields found in wind tunnels, and this method has been used here for the measurement of the (k_1, c) spectrum of wall pressure in a two-dimensional turbulent boundary layer in zero pressure gradient.

2. Theoretical discussion

The simplest quantity providing information on the convection of the wall pressure fluctuations in a homogeneous, stationary flow is the longitudinal space-time covariance

$$R_{pp}(\xi, \tau) = \overline{p(x,t).p(x+\xi, t+\tau)}, \tag{2.1}$$

and various definitions of convection velocity, in addition to that adopted by Willmarth & Wooldridge (1962), have been based on properties of $R_{pp}(\xi, \tau)$ (see Wills 1964). We can instead study the properties of the double Fourier transform of $R_{pp}(\xi, \tau)$ with respect to space and time,

$$\hat{S}_{pp}(k_1, \omega) = (2\pi)^{-2} \int_{-\infty}^{\infty} \int_{-\infty}^{\infty} R_{pp}(\xi, \tau).e^{ik_1\xi}.e^{i\omega\tau} d\xi\, d\tau, \tag{2.2}$$

and use this function to define the wave-number/phase velocity spectrum,

$$M_{pp}(k_1, c) = \hat{S}_{pp}(k_1, \omega), \tag{2.3}$$

where the phase velocity c is given by $c = -\omega/k_1$. The function $M_{pp}(k_1, c)$ contains the whole of the information in the complete $R_{pp}(\xi, \tau)$ correlation in a form which is particularly applicable to convected flows, as it shows the distribution of energy over the range of phase velocities for each wave-number, as well as giving the peak energy velocity for each wave-number, $U_c(k_1)$, defined by

$$\{\partial M_{pp}(k_1, c)/\partial c\}_{c=U_c(k_1)} = 0. \tag{2.4}$$

The function $M_{pp}(k_1, c)$ can most conveniently be obtained from the space correlation of signals filtered with narrow-band filters at frequency ω, $S_{pp}(\xi, \omega)$, by a single Fourier transformation

$$M(k_1, c) = (2\pi)^{-1} \int_{-\infty}^{\infty} S_{pp}(\xi, \omega).e^{ik_1\xi} d\xi, \tag{2.5}$$

since $S_{pp}(\xi, \omega)$ is effectively the Fourier transform with respect to τ of the space-time correlation $R_{pp}(\xi, \tau)$

$$S_{pp}(\xi, \omega) = (2\pi)^{-1} \int_{-\infty}^{\infty} R_{pp}(\xi, \tau).e^{i\omega\tau} d\tau. \tag{2.6}$$

As $R_{pp}(\xi, \tau)$ is not in general an even function of τ (except for $\xi = 0$), $S_{pp}(\xi, \omega)$ may be complex, having real and imaginary parts, say $S_{pp}(\xi, \omega)_R$ and $S_{pp}(\xi, \omega)_I$. In the practical case these correspond to the simultaneous filtered correlation and that measured with a time delay of $\pi/2\omega$, or a phase shift of $\frac{1}{2}\pi$ at frequency ω, in one of the signal channels.

Then since $R_{pp}(\xi, \tau) = R_{pp}(-\xi, -\tau)$, $S_{pp}(\xi, \omega)$ and $S_{pp}(\xi, \omega)_I$ will be even and odd respectively, so that

$$M(k_1, c) = (\pi)^{-1} \int_0^\infty S_{pp}(\xi, \omega)_R \cos k_1 \xi + S_{pp}(\xi, \omega)_I \sin k_1 \xi \, d\xi \tag{2.7}$$

and

$$M(k_1, -c) = (\pi)^{-1} \int_0^\infty S_{pp}(\xi, \omega)_R \cos k_1 \xi - S_{pp}(\xi, \omega)_I \sin k_1 \xi \, d\xi, \tag{2.8}$$

i.e. the downstream-travelling energy is the sum of the transforms of the real and imaginary parts of the filtered correlation, while the upstream-travelling energy is their difference. From this it can be seen that, if all the energy is known to be travelling in one direction, the contributions from the transforms of $S_{pp}(\xi, \omega)_R$ and of $S_{pp}(\xi, \omega)_I$ are identical, with a sign change if the energy is travelling upstream. In that case it would be sufficient to measure only $S_{pp}(\xi, \omega)_R$. At the other extreme, a standing-wave pattern (if that were dynamically possible), having equal energy at positive and negative velocities, would have $S_{pp}(\xi, \omega)_I = 0$. In an attached boundary layer the instantaneous velocity appears to be always positive, so that all the convection will be in the downstream direction. However, there may still be a contribution from acoustic waves that may travel in any direction (see § 5), so that the complete spectrum is still required.

In this experiment, the $M_{pp}(\mathbf{k}, c)$ spectrum has been measured in the longitudinal and lateral directions. (In the latter case, ξ in the above relations is to be replaced by ζ.)

3. Experimental equipment

The experiments were carried out in the NPL boundary-layer tunnel (described fully by Bradshaw & Hellens (1964)). The tunnel working section is 59 in. (1·5 m) wide by a nominal 9 in. (23 cm) high, the roof being adjustable to set the desired longitudinal pressure gradient. For these experiments, the roof was set to give zero pressure gradient at a free-stream velocity of 125 ft./sec (38 m/sec). The floor is of cast aluminium plates spanning the tunnel, with 3·5 in. (8·9 cm) diameter instrumentation disks set flush with the floor and spaced at 6 in. (15·2 cm) pitch along the tunnel centre-line. The upstream transducer was approximately 84 in. (2·13 m) from the leading edge of the floor plate, at a point where the boundary-layer thickness δ_{995} was 1·3 in. (3·3 cm). The velocity profile at this point is shown in figure 2.

Two types of transducer were used; one the conventional lead zirconate titanate piezo-electric type, the other developed specifically for small-separation correlation measurements from the orifice-hot-wire probe of Kovasznay & Remenyik (1962). The crystal transducers were 0·125 in. (0·32 cm) diameter, mounted flush with the surface and close to the edge of an 'Araldite' disk which

could be rotated to vary the separation between two such transducers. The disks were backed by heavy brass bodies resiliently mounted in the transducer casings to isolate the transducers from mechanical vibration of the tunnel floor. By using the transducers in different holes in the tunnel floor, the separation between the two measuring points could be varied continuously from 3·25 in. (8·25 cm) to 27 in. (69 cm) in the downstream direction, and from 3·25 in. (8·25 cm) to 15 in. (38 cm) in the lateral direction. The transducers were connected by short, low-noise coaxial cables to cathode followers with an input impedance of 100 MΩ, giving a low-frequency cut-off at about 25 Hz.

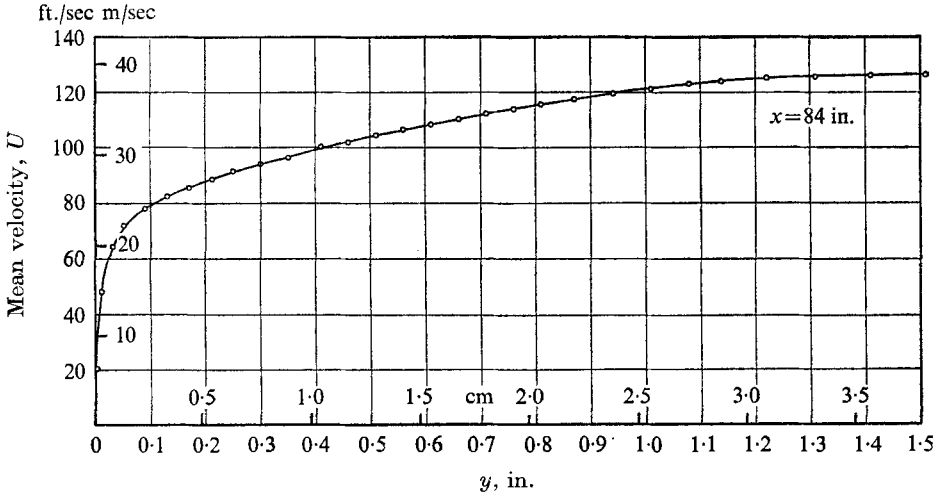

FIGURE 2. Boundary-layer velocity profile.

For all the correlations at small separations, an orifice-hot-wire probe pair was used. Figure 3 shows a sketch of the instrument, taken from Wills (1968*a*). The transducer diameter was 0·036 in. (0·92 mm), and covered the separation range 0·1–2·9 in. (0·25–7·4 cm). The hot wires were operated by Disa constant temperature anemometers.

The cathode follower or Disa anemometer output signals were amplified by Tektronix 122 low-noise pre-amplifiers and filtered by identical Brüel and Kjaer 2112 audio-frequency spectrometers on the $\frac{1}{3}$-octave bandwidth setting, before correlation by a time-division multiplier (Johnson 1962). The instantaneous product signal was integrated for a fixed time to yield the covariance signal. At higher frequencies, where there was some doubt that a $\frac{1}{3}$-octave filter was sufficiently narrow, a constant 200 Hz pass band was used. For the $S_{pp}(\xi, \omega)_I$ measurements, the output of one of the Tektronix pre-amplifiers fed a phase-shifter/differentiator network, giving a phase shift of $90° \pm 1°$ over the filter pass band at each of the chosen frequencies. The output of the phase shifter fed the Brüel and Kjaer spectrometer as before.

$S_{pp}(\xi, \omega)$ was measured at filter centre frequencies of 200, 400, 800, 1600 and 3150 Hz in the longitudinal direction, and $S_{pp}(\xi, \omega)_R$ was also measured at 100 Hz for comparison, although the range of separation required (> 30 in.)

means that the flow is no longer homogeneous. In the lateral direction, $S_{pp}(\zeta, \omega)$ was measured at frequencies of 200, 400, 800, 1600 and 3150 Hz ($S_{pp}(\zeta, \omega)_I$ is identically zero).

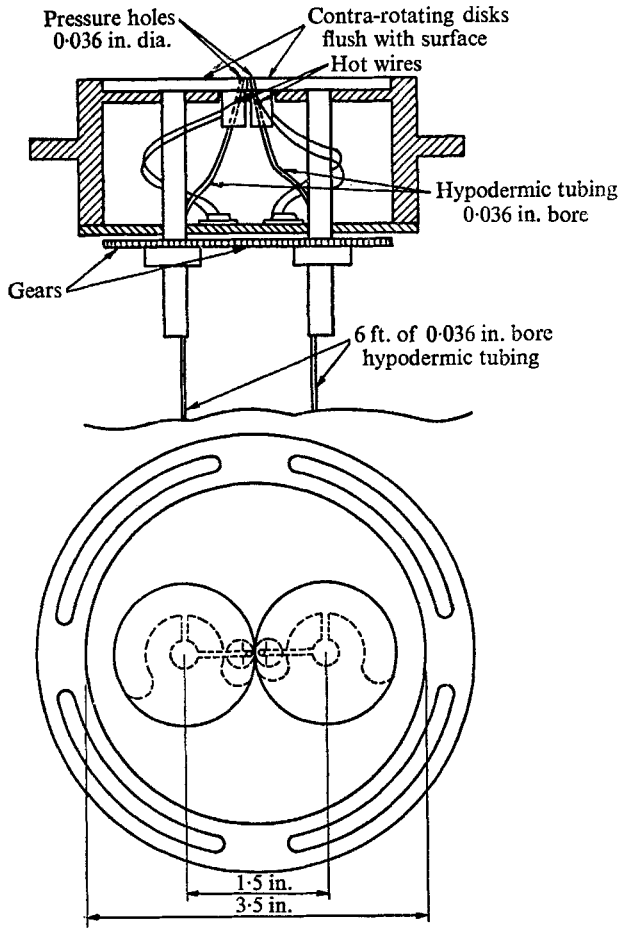

FIGURE 3. Orifice-hot-wire probe traversing gear.

4. Presentation of results

The longitudinal correlations $S_{pp}(\xi, \omega)_R$, normalized to unity at $\xi = 0$, are shown in figures 4(*a*)–(*b*) and $S_{pp}(\xi, \omega)_I$ in figure 5. The curves show the typical damped cosine and sine wave forms respectively, similar to those obtained by Harrison (1958) in a turbulent boundary-layer flow. In addition, the results at the lower frequencies, 100, 200 and 400 Hz, exhibit an appreciably non-zero correlation area, whereas the curves at higher frequency integrate more or less to zero. This non-zero area is thought to be due to extraneous sound in the wind tunnel, and will be discussed in §5. Similar results were found in the experiments of Willmarth & Wooldridge (1962), and forced the authors to exclude the low frequencies from their correlation measurements.

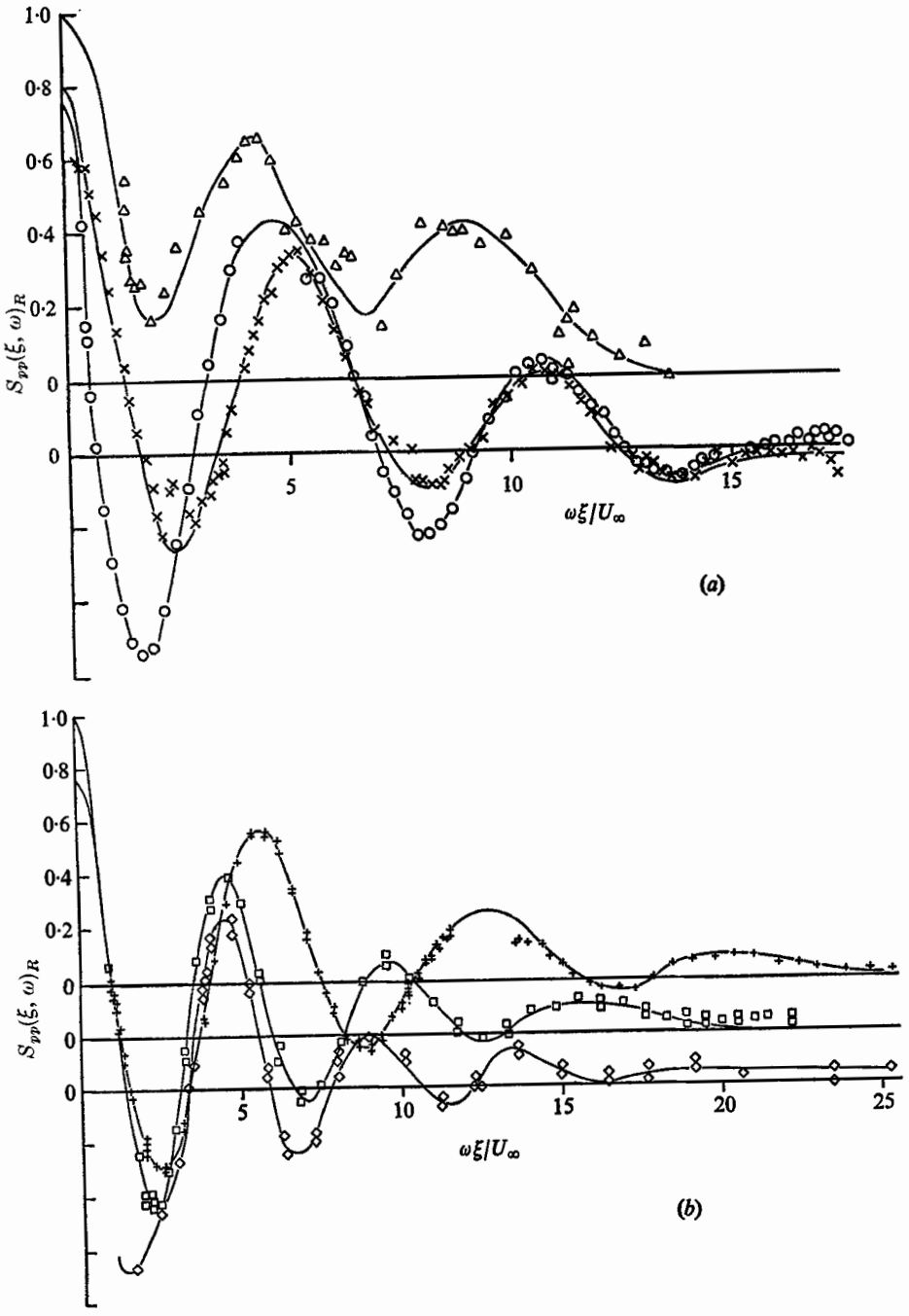

FIGURE 4. Longitudinal filtered spatial correlation. (*a*) △, f = 100 Hz; ×, f = 200 Hz; ○, f = 400 Hz. (*b*) +, f = 800 Hz; □, f = 1600 Hz; ◇, f = 3150 Hz.

The results for the filtered correlations with lateral separation are shown in figure 6. Here again there is evidence of extraneous sound at 200 and 400 Hz, where the correlations tend to a non-zero limit at large separations.

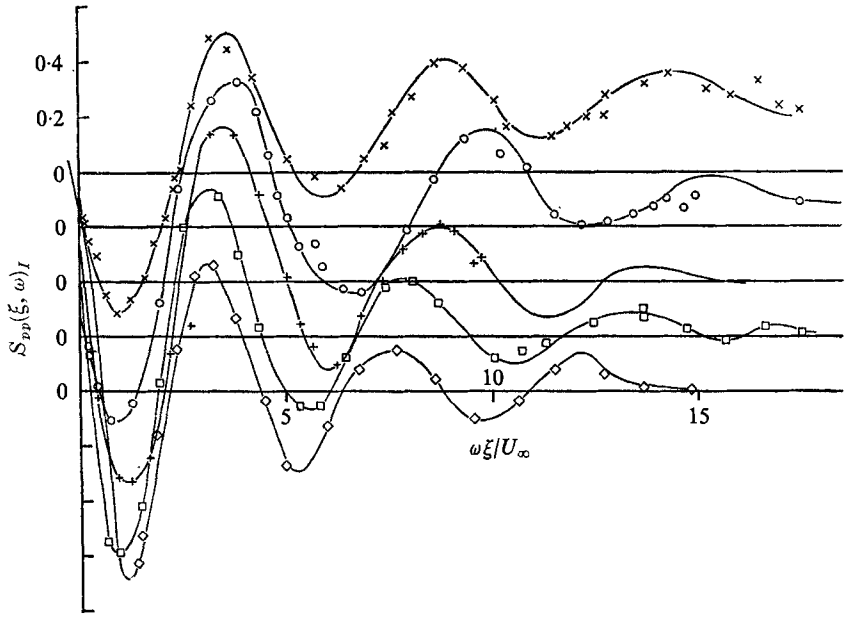

FIGURE 5. Longitudinal imaginary filtered spatial correlation. ×, f = 200 Hz; ○, f = 400 Hz; +, f = 800 Hz; □, f = 1600 Hz; ◇, f = 3150 Hz.

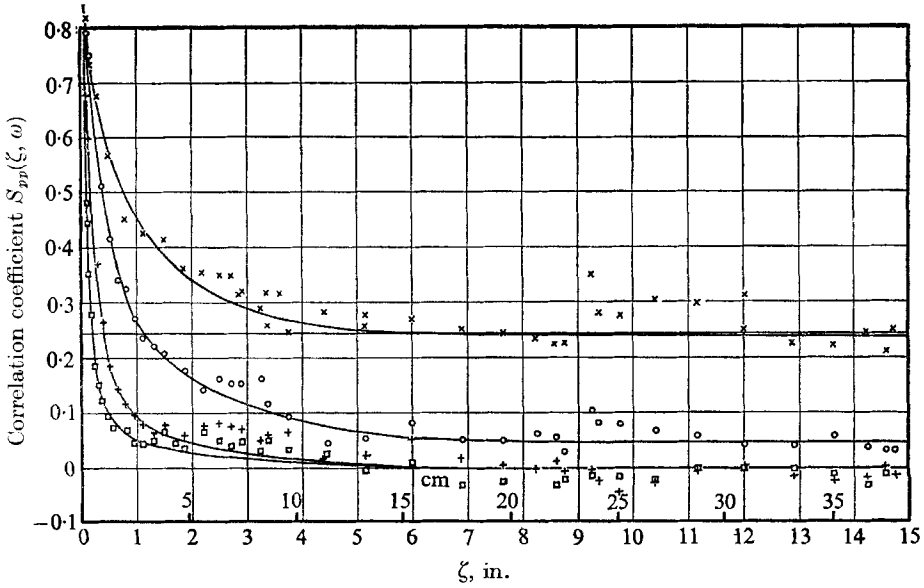

FIGURE 6. Lateral filtered spatial correlations. ×, 200 Hz; ○, 400 Hz; +, 800 Hz; □, 1600 Hz.

5. Extraneous sound

In the experiments of Willmarth & Wooldridge (1962), in the present experiment (figure 8) and in many other low-speed wind tunnel experiments, the frequency spectrum of the wall pressure rises sharply at low frequencies. As the precise shape of the low-frequency spectrum varies in different experiments, it seems likely that the low-frequency rise is due to the conditions of the experiment and not to the boundary layer itself.

Willmarth & Wooldridge filtered out frequencies below 105 c/s ($\omega\delta^*/U_\infty = 0{\cdot}14$), the point at which the low-frequency rise began, from their measurements of $R_{pp}(\xi, \tau)$. The results that they obtained showed, in addition to the peaks corresponding to the downstream-convected turbulence, small peaks corresponding to a disturbance travelling upstream at about the speed of sound. When the high-pass filter cut-off frequency was increased to 300 c/s ($\omega\delta^*/U_\infty = 0{\cdot}41$), these small peaks disappeared.

It thus appears that at least part of the low-frequency pressure fluctuation arises from sound waves in the working section, and a similar result has been found in the present experiment. Consider the lateral correlation at 200 Hz; it falls to a constant value of 0·25 at large separations, suggesting a plane wave correlated right across the tunnel. Kraichnan (1956) has shown that

$$\hat{S}_{pp}(\mathbf{k}, \omega)_{\mathbf{k}\to 0} = 0. \tag{5.1}$$

Thus the area under the $S_{pp}(\xi, \zeta, \omega)$ curves should be zero in incompressible flow. For $\xi = 0$, the results of figure 6 show that $S_{pp}(\zeta, \omega) \geqslant 0$ for all ζ, even with the asymptotic low-frequency correlations subtracted, so that to satisfy condition (5.1) it seems likely that

$$\int_{-\infty}^{\infty} S_{pp}(\xi, \omega)\, d\xi$$

will be small in incompressible flow. The contribution from the turbulence/mean shear term alone is identically zero (see Lilley & Hodgson 1960).

The fact that, for instance, the $S_{pp}(\xi, \omega)_R$ curve at 200 c/s, figure 4(*a*), and the corresponding $S_{pp}(\xi, \omega)_I$ curve, figure 5, have a positive correlation area taken over a large separation range is thus taken to imply the presence of acoustic waves in the wind tunnel. (This is not to suggest that the correlation area taken over sufficiently large separation will not be zero, but merely that the correlation contains a large-scale component whose wavelength is comparable with the correlation length of the boundary-layer turbulence.) Inspection of figure 5 indicates that the waves are travelling upstream, since the large-scale correlation is of opposite sign to that of the downstream-travelling turbulence correlation. Thus if we assume acoustic waves correlated across the working section, and travelling upstream at a speed $(a_0 - U_\infty)$, with a mean square intensity of 0·25 of the total correlation at 200 Hz, given by the asymptotic correlation in figure 6, we can subtract the acoustic contribution from the turbulence contribution. This has been done in figure 7 for the $S_{pp}(\xi, \omega)_R$ and $S_{pp}(\xi, \omega)_I$ curves at 200 Hz, and it can be seen that the residual area under the curves is quite small. Similar good agreement is obtained at 400 Hz, for an acoustic contribution of 0·1 to the mean

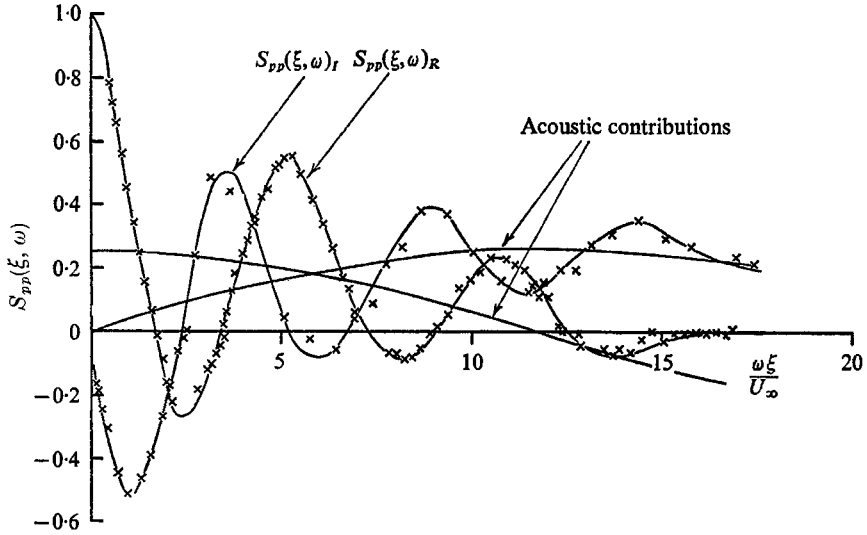

FIGURE 7. Longitudinal correlations $f = 200$ Hz.

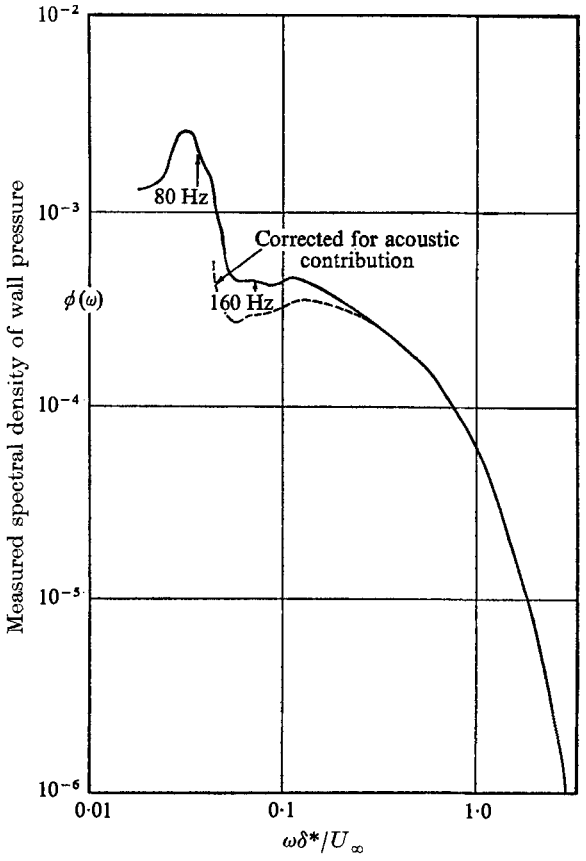

FIGURE 8. Frequency spectrum of boundary-layer wall pressure.

square pressure, while for the $S_{pp}(\xi, \omega)_R$ correlation at 100 Hz, figure 4(*a*) suggests an acoustic contribution of 0·5. No results are available at lower frequencies, because of the prohibitively large separation distances involved, but from the rate at which the acoustic contribution increases with decreasing frequency one might guess that nearly the whole of the contribution below 100 Hz is acoustic. Figure 8 shows the pressure frequency spectrum measured with the 0·125 in. transducer, normalized with respect to frequency ω, together with the correction for the acoustic contribution. The peaks at 80 and 160 Hz correspond to the fan first and second harmonics, but the remainder of the acoustic contribution appears to be wide-band in nature. Since it is propagating upstream, the most likely source appears to be unsteadiness in the flow in the first diffuser. This suspicion has been confirmed by some later measurements made in a simple blower tunnel with and without a straight rectangular diffuser with an equivalent conical total angle of 5° (Wills 1968*b*). The spectral density at low frequencies was reduced by a factor approaching 100 when the diffuser was removed.

The advantage of the $M_{pp}(k_1, c)$ spectrum approach is that the acoustic contribution can readily be isolated even at low frequencies, whereas with the $R_{pp}(\xi, \tau)$ approach, it is necessary to discard the whole of the low-frequency contribution, as previous workers have done. In this case, it is difficult to estimate the effect of removing the low frequencies on the overall space-time correlation. Using the (k_1, c) approach, neglect of the low (or high) frequencies results only in a lack of data in limited regions.

6. Other corrections

In a similar way, the (k_1, c) approach allows corrections to be made for finite filter bandwidth and transducer size. The effect of using a filter of finite bandwidth with uniform response over the band amounts to averaging the energy over the filter bandwidth at constant wave-number, i.e. that

$$M_m(\mathbf{k}, -c) = \int_{\omega_1}^{\omega_2} M(\mathbf{k}, -c)\, d\omega, \tag{6.1}$$

where ω_1 and ω_2 are the limits of the filter bandwidth. Similarly, for a non-uniform filter response, the measured spectrum will be the integral of the product of the true spectrum at constant wave-number and the filter response.

It is also possible to allow for the effect of finite transducer size on the measurements. The pressure transducer will average the instantaneous pressure over its surface area, and thus gives a reduced output at high wave-numbers. For the case of a transducer having an output signal linear with pressure, the analysis of Uberoi & Kovasznay (1953) shows that the wave-number response $S(\mathbf{k})$ of the transducer (analogous to the frequency response of a time-dependent instrument) is given by the Fourier transform of the convolution of the spatial response of the transducer $K(s)$ with $K(-s)$, i.e.

$$S(\mathbf{k}) = \int\int e^{i\mathbf{k}.\mathbf{r}} K(-\mathbf{s})\, K(\mathbf{r}-\mathbf{s})\, d\mathbf{s}\, d\mathbf{r}. \tag{6.2}$$

For a circular pressure transducer $S(\mathbf{k})$ reduces to the square of the Hankel transform

$$\int_0^\infty J_0(kr) r K(r)\, dr$$

of the spatial sensitivity function $K(r)$, where $k = |\mathbf{k}|$ and r is the radial distance, and for a transducer having constant response inside the circle and zero outside, the mean square wave-number response becomes

$$S(k) = \left[\frac{2J_1(ka)}{ka}\right]^2, \tag{6.3}$$

where a is the transducer radius and J_1 is the Bessel function of the first order (figure 18). The measured $(\mathbf{k}, c)$ field, $M_m(\mathbf{k}, c)$, is then given by

$$M_m(\mathbf{k}, c) = S(k) M(\mathbf{k}, c). \tag{6.4}$$

The corrections to be applied to experimental results will be discussed in § 7 in the light of the measurements obtained here.

7. Discussion of results

The Fourier transforms of the longitudinal and lateral correlation curves were evaluated numerically on the NPL KDF 9 digital computer, using a 101-point linear interpolation method. Figure 9 shows the transform of the 200 Hz longitudinal correlation, where the acoustic component shown in figure 7 has been subtracted from the correlations. The curves are the sum and difference of the transforms of $S_{pp}(\xi, \omega)_R$ and $S_{pp}(\xi, \omega)_I$, representing the energy travelling with positive and negative velocities respectively, and the values of $\hat{S}_{pp}$ are normalized with respect to k and ω, i.e. $\iint \hat{S}_{pp}(k_1, \omega) dk,\ d\omega = 1$. The fact that there is an apparent secondary peak in the negative velocity direction at $k_1 \delta \doteqdot 1$, with an amplitude of 0·2 of the main peak, is not thought to be significant, and is probably due to phase differences between the two filter responses. The apparent secondary peak was much smaller at higher frequencies where the filters were known to be better matched. In an acoustic field, the negative-velocity components could be attributed to a standing-wave pattern, but since there is no mechanism by which the turbulent flow can support upstream-travelling waves at the observed velocity, this explanation must be rejected in this case. Any true negative-velocity energy would be found only at low negative velocities (large k_1) and would be expected to decrease in intensity with decreasing k_1. The inaccuracy of the numerical transforms at large k_1 makes it difficult to study this region, but no evidence was found of upstream-travelling energy apart from the low-frequency acoustic waves. Accordingly, no attempt has been made to incorporate the apparent negative-velocity components into the complete (k_1, ω) plots.

Figure 10 shows a contour plot of the (k_1, ω) spectrum, representing the sum of the transforms of $S_{pp}(\xi, \omega)_R$ and $S_{pp}(\xi, \omega)_I$. The results at low k_1 and low ω here have been excluded from this plot, partly because they represent a sound field, but mainly because the computed k_1 spectra are inaccurate at low values of k_1 because of the need to truncate the filtered space-correlations at large separations. The working section length is only two wavelengths of sound at 200 Hz.

The strong convection of the fluctuations, shown by the concentration of energy into a diagonal band in figure 10, is shown more clearly in figure 11, a contour plot of $M_{pp}(k_1, c)$. The convection velocity $U_0(k_1)$ defined by equation (2.4) as the peak-energy velocity at constant k_1, is shown by the dotted line through the peaks of the contours. $U_c(k_1)$ is seen to vary from a maximum value of about $0{\cdot}9\,U_\infty$ at a value of $k_1\,\delta_{995}$ equal to 1·2, to an asymptotic value of $0{\cdot}55\,U_\infty$ at high k_1.

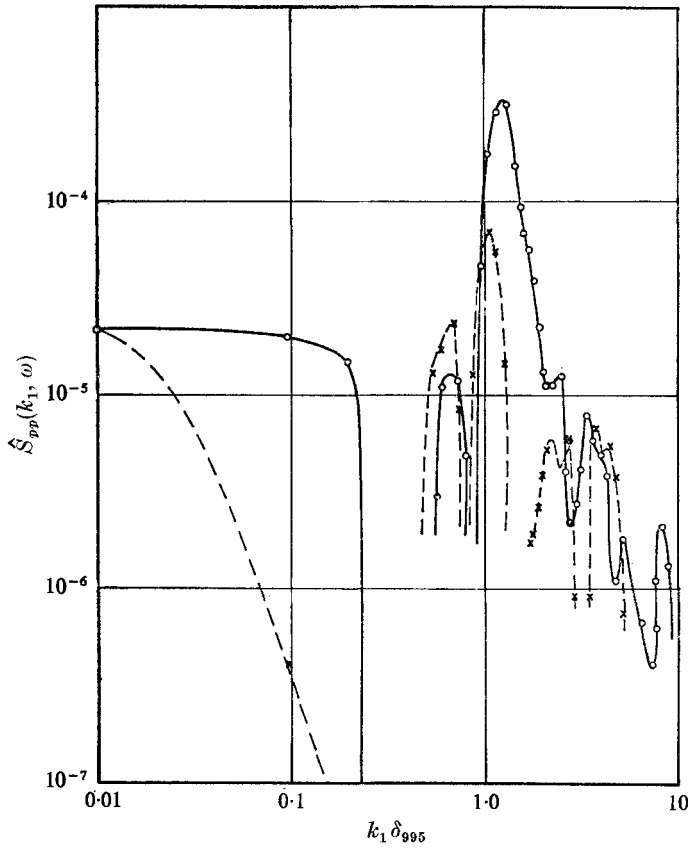

FIGURE 9. Measured longitudinal wave-number spectrum at $f = 200$ Hz.
—, $\phi_1(k_1, \omega)$; - - - -, $\phi_1(k, -\omega)$.

This variation of $U_c(k_1)$ demonstrates the fact that the largest eddies extend over the whole width of the boundary layer and are convected with speeds typical of the outer layer, while those small-scale eddies contributing to the wall pressure are situated close to the wall and are therefore convected with lower velocities.

This high-wave-number convection velocity falls well below that, for example, of Willmarth & Wooldridge (1962). The reason is that the usual definition of convection velocity is weighted towards that of the most energetic wave-numbers. What is at first sight surprising is the comparatively low wave-number

$$(k_1\,\delta_{995} = 20)$$

at which the asymptotic value is attained, i.e. when the wavelength is less than

one quarter the boundary-layer thickness. It is interesting to note that the wave guide models of Landahl (1967) and others (Sharma 1968) also predict phase velocities that are consistently lower than the conventional convection velocity in this range of wave-numbers. Figure 12 shows a comparison between the values of $U_c(k_1)$ obtained here and the predicted phase velocity of the least damped wave in Landahl's model. The agreement is excellent at higher wave-numbers, but at

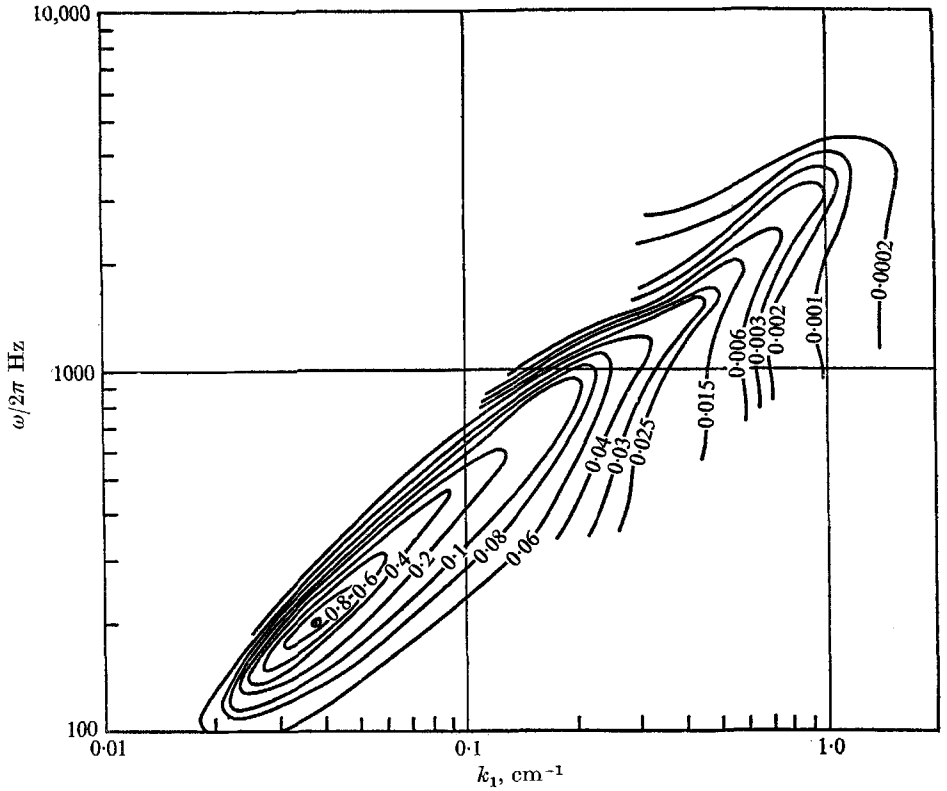

FIGURE 10. Contour plot of $\hat{S}_{pp}(k_1, \omega)$.

low wave-numbers $U_c(k_1)$ rises above the predicted values. This may reflect the fact that the large-scale energetic motion cannot be regarded as a perturbation on a mean profile. Figure 12 also shows a comparison of theoretical and experimental decay coefficients. Experimental values are difficult to define because the experimental curves do not exhibit exactly the logarithmic decay of amplitude predicted by the theory. The experimental values represent an approximate fit to a logarithmic decay and are thus rather scattered, but the agreement is still remarkably good.†

At the lowest wave-numbers, $U_c(k_1)$ appears to decrease again, but the inaccuracy of the experimental results at 100 Hz (figure 4(*a*)) make it difficult to be sure that this is a significant result. Bradshaw (1967) found a similar behaviour at

† In a private communication, Professor Landahl has pointed out that with the more practical assumption of waves inclined at 60° to the flow, the agreement is almost perfect.

low wave-numbers in a boundary layer in adverse pressure gradient, although in that case the effect was plausibly attributed to the streamwise inhomogeneity of the flow. In the present experiments, the inhomogeneity is restricted to a slight increase in boundary-layer thickness with distance downstream, amounting to only $\delta/30$ over one turbulence wavelength at 100 Hz, an amount which must be too small to account for the apparent reduction of $U_c(k_1)$ at low wave-number. If the reduction is real its explanation must lie elsewhere.

Inspection of the computed transforms reveals that in the region of significant energy the wave-number spectra are similar at all frequencies measured, within experimental accuracy, so that the height of the main peak of the wave-number

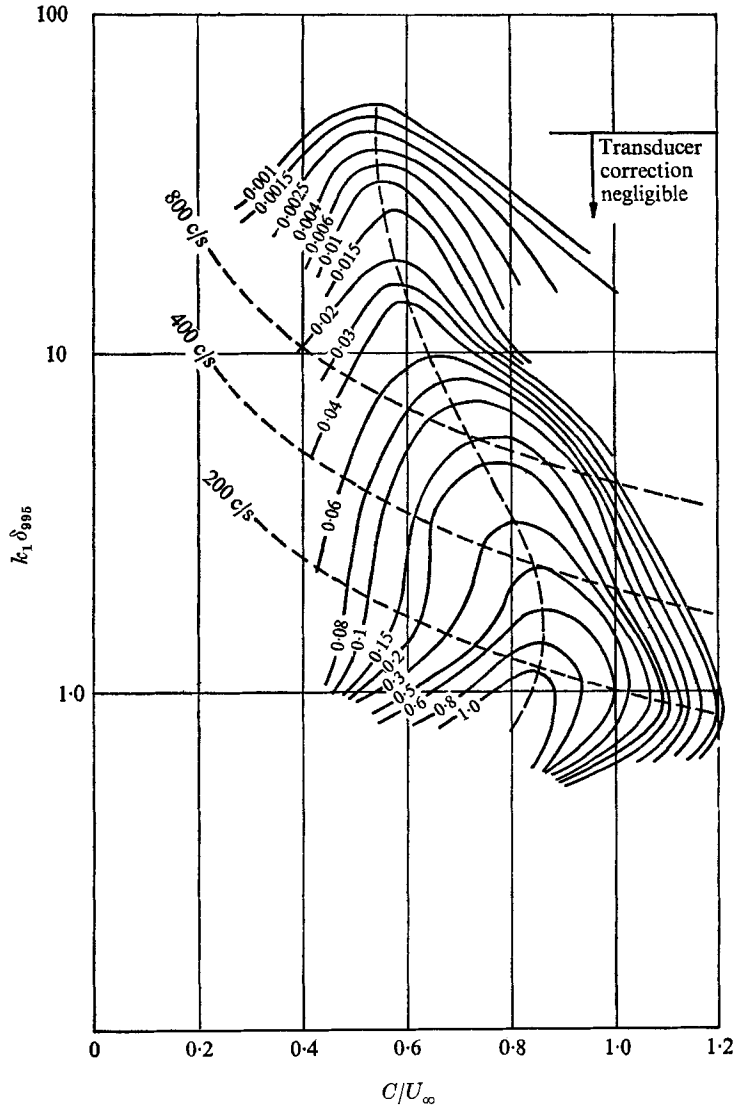

FIGURE 11. Contour plot of $M_{pp}(k_1, c)$. $U_c(k_1)$ given by $\{\partial M_{pp}(k_1, c)/\partial c\}_{c=U_c(k_1)} = 0$.

spectrum is proportional to the integrated spectral density at each frequency. Thus the complete (k_1, ω) spectrum can be approximated by

$$\hat{S}_{pp}(k_1, \omega) \doteq \Phi(\omega) F\left(\frac{\omega}{k_1 U_\omega}\right), \tag{7.1}$$

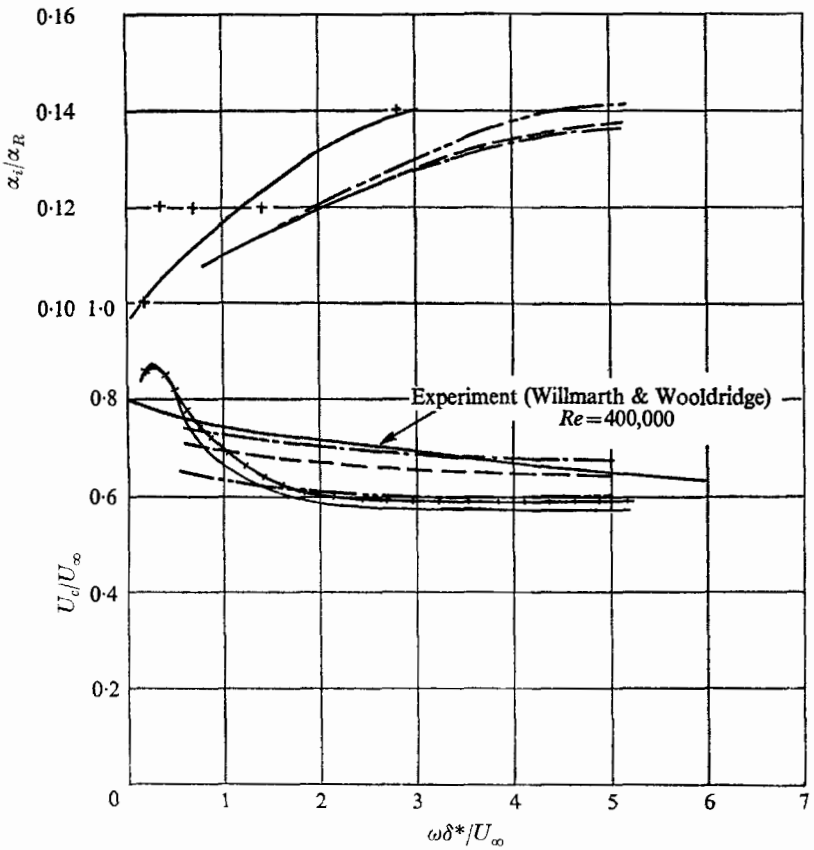

FIGURE 12. Comparison with model of Landahl (1967). Theory (Landahl): — · —, Re = 5000; – – –, Re = 10,000; — · · —, Re = 40,000. Experiment (Wills): +++++, Re = 70,000, U_ω/U_∞; —, Re = 70,000, U_c/U_∞.

where $\Phi(\omega)$ is the frequency spectrum, and U_ω is a convection velocity varying with frequency, also plotted in figure 12. This result implies that the filtered space correlation is of the form

$$R_{pp}\left(\frac{\omega\delta_{995}}{U_\omega}\right),$$

as can be seen from figures 4(*a*)–(*b*), and has been found by Corcos (1962) and others. Figure 13 shows the function F of equation (7.1), obtained from a smoothed curve through the results of figure 9 (although, since the transforms are similar, F could equally well have been taken from the transform at another frequency). The results fit a normal distribution curve

$$\exp\left[-(\omega\delta_{995}/U_\omega - 1)^2/0{\cdot}2^2\right]$$

very closely except at small values of the argument. Thus the phase velocity at constant frequency is a nearly normal distribution with a standard deviation of $0{\cdot}14\,U_\omega$. The corresponding result in the adverse-pressure-gradient boundary layer of Bradshaw (1967) is $0{\cdot}21\,U_\omega$. These results support the intuitive idea of the smaller eddies being disturbed randomly from the local mean velocity by the large-scale eddies, the standard deviation of the disturbance being of the order of the local turbulence level.

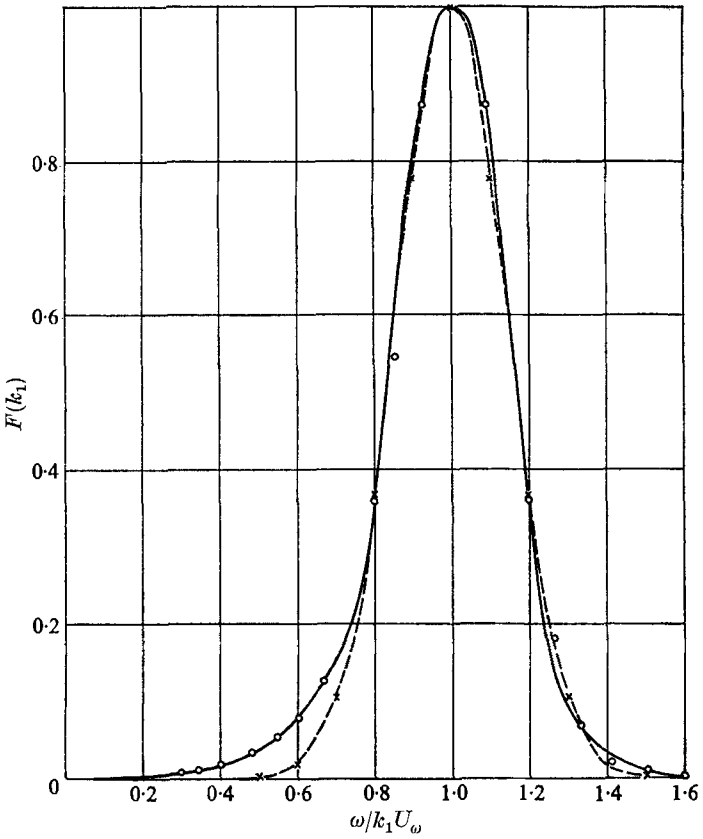

FIGURE 13. Function $F(\omega/k_1U_\omega)$ of equation (7.1), ω = constant. ×, $\exp\{-[\omega/k_1U_\omega-1]^2/0{\cdot}2^2\}$; ○, $F(k_1)$.

Figure 14 shows the Fourier transforms of the lateral correlations of figure 6, where the large-scale acoustic contribution at 200 and 400 c/s has been subtracted from the correlations before evaluating the transforms. Corcos (1962), using the more limited experimental data of Willmarth & Wooldridge (1962), suggested that the lateral filtered correlations, $S_{pp}(\zeta,\omega)$, should collapse on a single curve when plotted against $\omega r_3/U_\omega$, and this implies that $\hat{S}_{pp}(k_3,\omega)$, the Fourier transform of $S_{pp}(\zeta,\omega)$, should collapse on $k_3\,U_\omega/\omega$. However, in this experiment the results did not collapse on this parameter. In particular, the wave-number spectrum at the higher frequencies is noticeably flatter than at low frequencies. Bradshaw (1967) argues the collapse of $\hat{S}_{pp}(k_3,\omega)$ when plotted against k_3U_ω/ω

for the higher wave-numbers, on the basis of inner layer similarity, but such similarity would be centred on a value of $k_3\delta$ of about 40 in the present experiment, close to the experimental limit imposed by the finite minimum separation of the transducers. Thus the experiments cannot provide verification of the lateral scaling parameter at high frequencies where dimensional considerations lead us to expect that it might hold, but show that the scaling does not hold at the lower frequencies. A more direct check of inner-law scaling is discussed in §8.

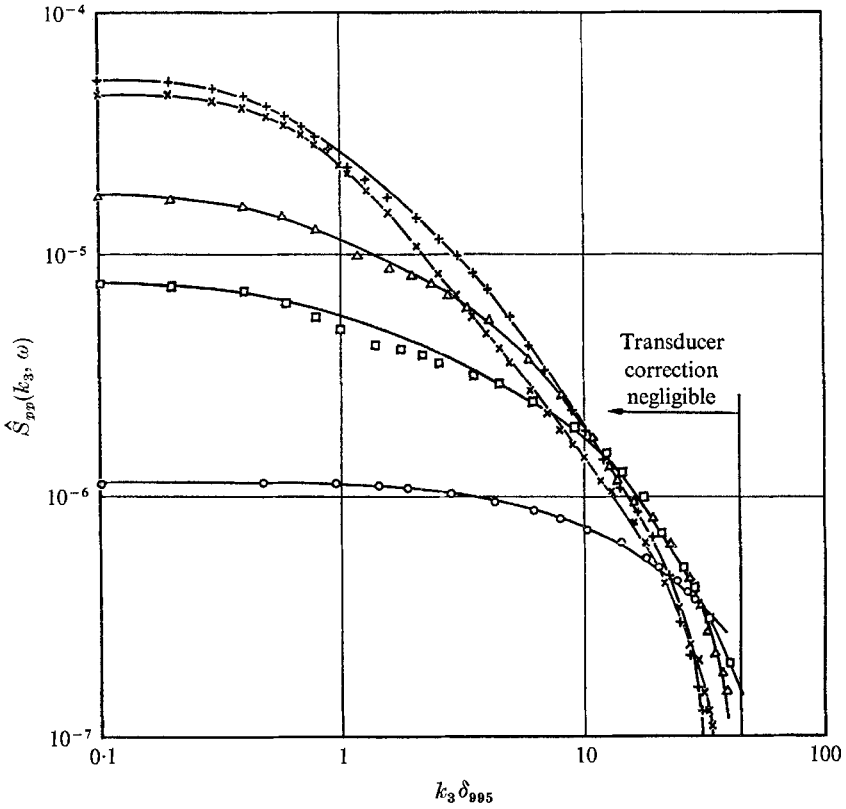

FIGURE 14. Measured lateral wave-number spectra. ×, 200 Hz; +, 400 Hz; △, 800 Hz; □, 1600 Hz; ○, 3150 Hz.

Because the turbulence level in the boundary layer is of the order of $0{\cdot}1\,U_\infty$, we would expect the phase velocities associated with the cross-stream convection to be of the order of $\pm 0{\cdot}1\,U_\infty$, while the phase velocities associated with the downstream convection are, as we have seen, of the order of $U_c \pm 0{\cdot}1\,U_\infty$. Thus the contributions from the convection of the k_3 components, which fall off fairly rapidly with increasing k_3, are expected to appear only at low frequencies, so that the contribution to $\hat{S}_{pp}(k_3, \omega)$ at middle and high frequencies can mainly be attributed to the convection of the k_1 components. This property has been used here to convert the (k_3, ω) spectrum to an approximate (k_1, k_3) spectrum. The simplest assumption that can be made is that the energy at a longitudinal wave-number k_1 is rigidly convected at velocity U_c to produce an apparent frequency

$k_1 U_c$, i.e. that the (k_1, k_3) spectrum, $\psi(k_1, k_3)$, is given by

$$\psi(\omega/U_c, k_3) = \hat{S}_{pp}(k_3, \omega). \tag{7.2}$$

Figure 15 shows contours of ψ based on this assumption.

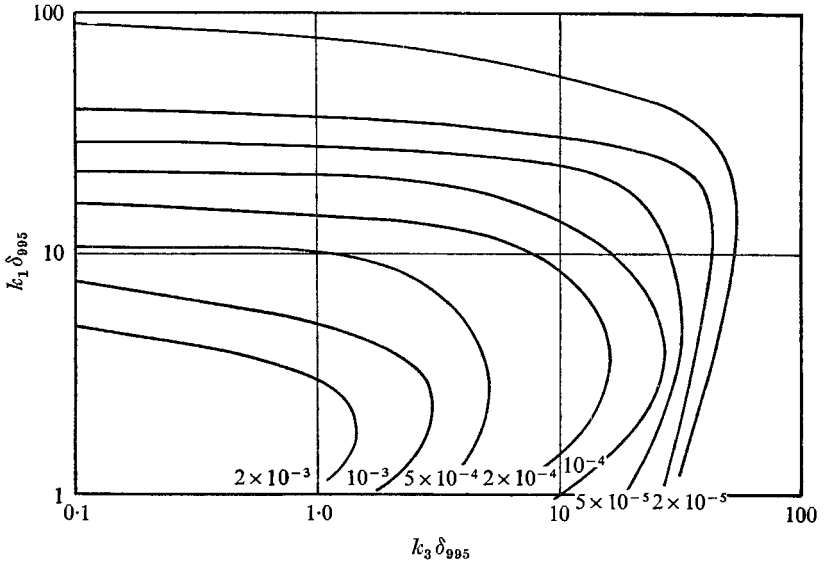

FIGURE 15. Contour plot of $\psi(k_1, k_3)$ based on equation (7.2). $\psi(k_1, k_3) = \hat{S}_{pp}(k_3, k_1 U_c)$.

A slightly more plausible form for the (k_1, k_3) spectrum is obtained by abandoning the rigid-convection assumption to relate the ω and k_1 spectra, and assuming instead that the distribution of energy over k_1 at a given frequency ω at each value of k_3 is the same as that for the integral over k_3 given by the function F of figure 13. The (k_1, k_3) spectrum is then given by

$$\psi(k_1, k_3) = \int_0^\infty \hat{S}_{pp}(k_3, \omega) F\left(\frac{\omega}{k_1 U_\omega}\right) d\omega. \tag{7.3}$$

Contours of $\psi(k_1, k_3)$ on this assumption are shown in figure 16.

Equation (7.3) appears to be a plausible assumption for the (k_1, k_3) spectrum, and a method of checking its accuracy is discussed in §8. If it is an accurate assumption, then figure 16 shows that at moderate wave-numbers there is about twice as much energy in the downstream component as in the lateral component. At the highest measurable wave-numbers the distribution is tending towards the isotropic form.

8. Frequency spectrum correction for transducer size

Equation (7.3) amounts to assuming that the more general spectrum $\hat{S}_{pp}(\mathbf{k}, \omega)$ is given by

$$\hat{S}_{pp}(\mathbf{k}, \omega) = \hat{S}_{pp}(k_3, \omega) F\left(\frac{\omega}{k_1 U_\omega}\right) \tag{8.1}$$

(which is also consistent with (7.1)). It is difficult to find means of checking the accuracy of (8.1) without measuring $\hat{S}_{pp}(\mathbf{k}, \omega)$ or $\psi(k_1, k_3)$, either of which would involve a lengthy experimental programme, but some sort of check can be made by using (8.1) and the transducer size correction, (6.3), to predict the spectral density $\Phi_m(\omega)$ measured with rather large transducers.

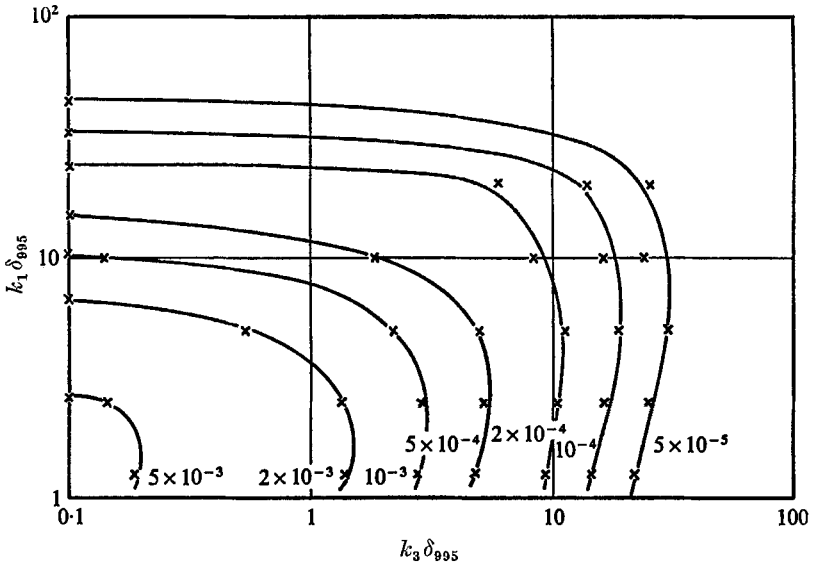

FIGURE 16. Contour plot of $\psi(k_1, k_3)$ based on equation (7.3).
$\psi(k_1, k_3) = \int \hat{S}_{pp}(\omega, k_3) F(\omega/k_1 U_\omega) d\omega.$

$\Phi_m(\omega)$ was measured with the 0·036 in. (0·91 mm) diameter orifice probe, the 0·125 in. (0·32 cm) crystal transducer, and also with Brüel and Kjaer $\frac{1}{4}$ in. and $\frac{1}{2}$ in. condenser microphones. The results are shown in figure 17, and also include some unpublished data of Hodgson (private communication) obtained with a 0·005 in. (0·13 mm) diameter probe microphone which should respond to the true wall pressure up to values of $\omega\delta^*/U_\infty$ greater than 10. It can be seen that the 0·036 in. (0·91 mm) diameter orifice probe responds to the true pressure up to $\omega\delta^*/U_\infty \doteqdot 3$, corresponding to a frequency of 6 KHz. We may also assume (see figure 18) that the true wave-number spectrum is recorded for wave-numbers up to $ka = 1$, corresponding to $k\delta_{995} = 60$. Since it is the loss of spatial resolution that leads to attenuation of the high frequencies, we may conclude that there is no contribution at frequencies below $\omega\delta^*/U_\infty = 3$ from wave-numbers above $k_1\delta_{995} = 60$. Thus we may assume that the orifice probe measures the true spectrum $\phi(\omega)$ for frequencies up to $\omega\delta^*/U_\infty = 3$, and may use these results and those obtained with the larger transducers to obtain the transducer size corrections. Predicted values of $\Phi_m(\omega)$ are given by

$$\Phi_p(\omega) = \int_{-\infty}^{\infty}\int_{-\infty}^{\infty} \hat{S}_{pp}(k_3, \omega) F\left(\frac{\omega}{k_1 U_\omega}\right) S(\mathbf{k}) dk_1 dk_3, \tag{8.2}$$

where $S(k)$ is the sensitivity function of the transducer. It was thought that, for the purpose of comparing a spectrum computed from a model such as (8.1) with

the experimentally measured spectrum, it would be necessary to use a true sensitivity function $S(\mathbf{k})$ for the particular transducer involved, rather than some idealized response such as (6.3). Gilchrist & Strawderman (1965) measured the spatial response $K(s)$ of two circular commercial lead zirconate transducers by applying a point load at different radii, and determined the 'effective' radius of the transducers, that is the radius of an ideal transducer having uniform

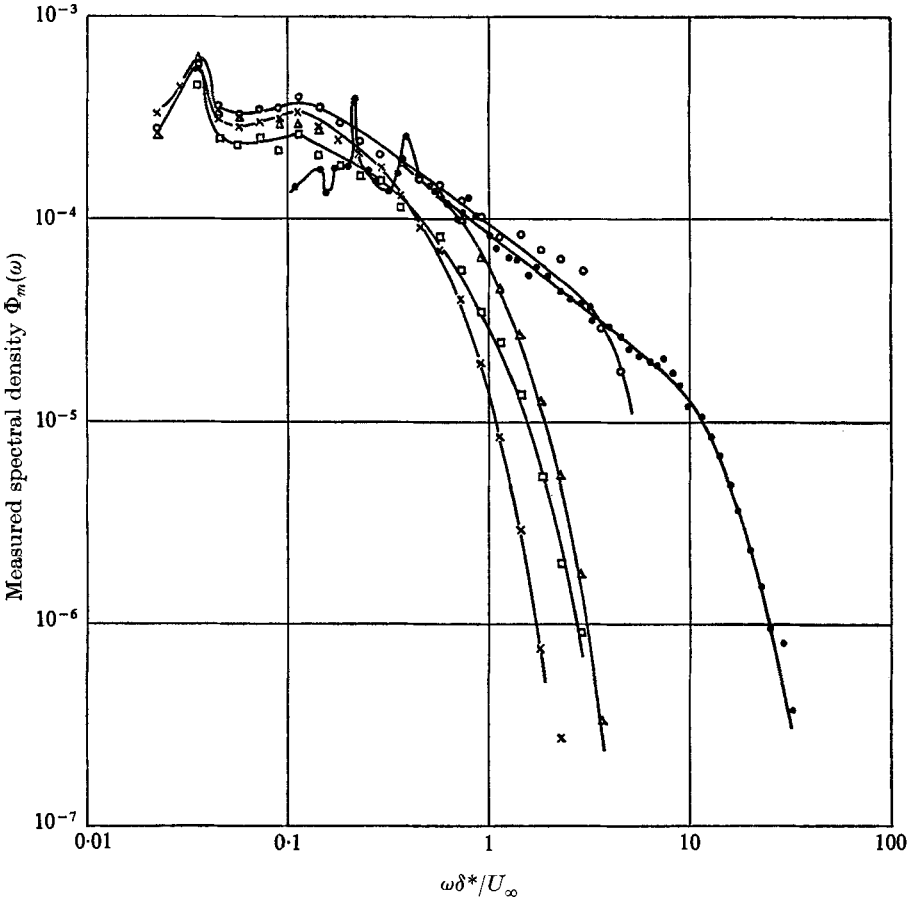

FIGURE 17. Wall pressure spectrum measured with various sized transducers. ○, orifice probe, 0·036 in. diameter; □, crystal transducer, 0·125 in. diameter; △, ×, Brüel & Kjaer microphone, 0·25 in. and 0·5 in. diameter respectively; ●, probe microphone, 0·005 in. diameter (Hodgson, private communication).

response inside the effective radius, equal to the average peak response near the centre of the real transducer, and zero response outside this radius. The radius was then chosen to make the overall sensitivity of the ideal transducer equal to that of the real transducer. Although this approximation may be expected to be reasonably accurate for sensitivity functions close to the ideal, there is no guarantee that it will give an accurate representation of $S(k)$ for other types of

sensitivity function. It was therefore decided to use values of $S(k)$ obtained by numerically evaluating the Hankel transform of actual sensitivity functions $K(s)$.

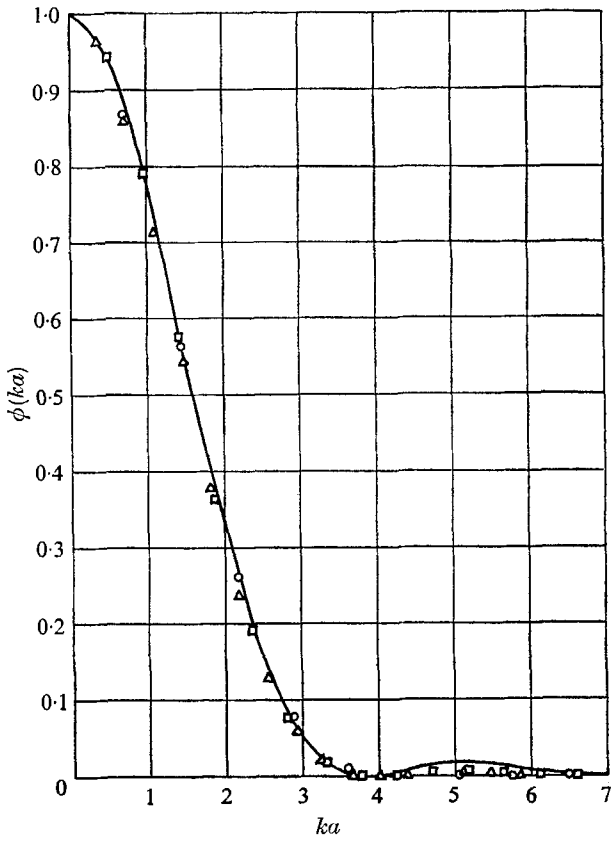

FIGURE 18. Computed wave-number response of transducers. —, $\{2J_1(ka)/ka\}^2$; ○, B & K 4131, effective radius 7·2 mm; □, LC 70, effective radius 2·36 mm; △, LD 107, effective radius 0·91 mm.

In the absence of facilities for making accurate measurements of $K(s)$ for the different transducers used in this investigation, the measured sensitivity function of Gilchrist & Strawderman (1965) was used for the $\frac{1}{8}$ in. crystal transducer, by scaling the radii of the two transducers. Sensitivity functions for the Brüel and Kjaer $\frac{1}{4}$ in. and $\frac{1}{2}$ in. microphones were obtained by scaling results obtained for a 1 in. microphone of similar geometry by Brüel & Rasmussen (1959). In this case the sensitivity function was measured by applying an oscillating localized electric field from a point electrode to the front face of the microphone diaphragm, at various radii. The resulting deflexions of the microphone diaphragm yield $K(s)$.

The numerically evaluated Hankel transforms of these sensitivity functions were then compared with that for the idealized transducer, equation (6.3), and it was found that, at least up to the first zero of (6.3) at $ka = 3{\cdot}83$, the wave-number response $S(k)$ for the real transducers compared very closely with (6.3) provided that an effective radius somewhat smaller than the true radius was chosen. In

fact, for the two transducers tested by Gilchrist & Strawderman (Atlantic Research Corporation LC-70 and LD-107), the effective radius obtained by comparing the wave-number responses compared closely with that obtained by the authors' method of comparing spatial sensitivity functions. Figure 18 compares the computed wave-number responses with the ideal response $(2J_1(x)/x)^2$ for effective radii 0·72, 0·73 and 0·69 of the actual radii for the B & K 4131,

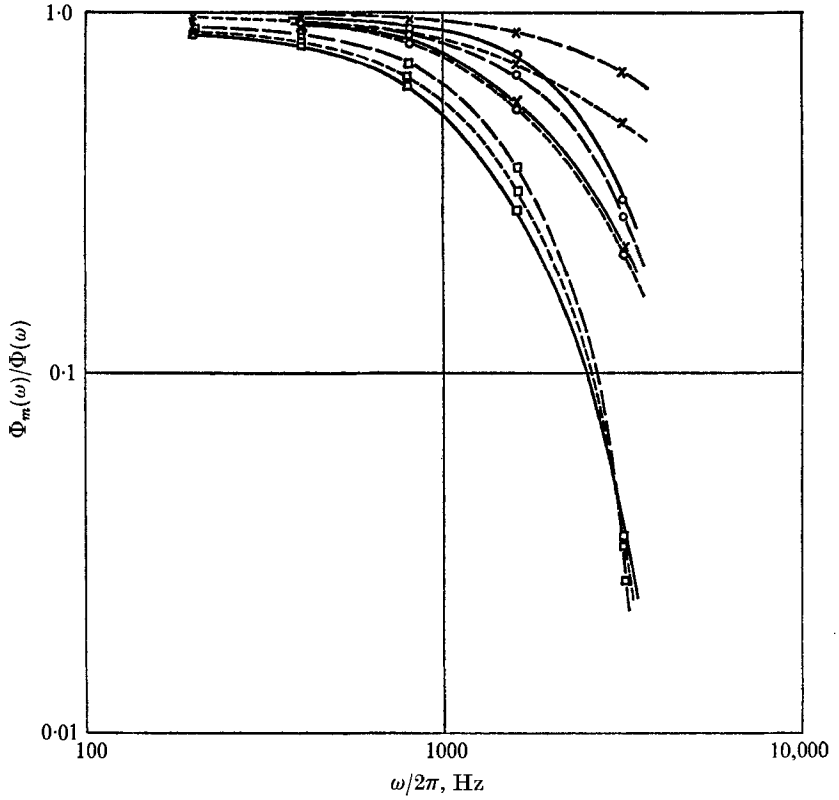

FIGURE 19. Comparison of measured and computed spectra. —, experiment; – – –, computation; - - - - -, Corcos correction; ×, $\frac{1}{8}$ in. crystal transducer; ○, $\frac{1}{4}$ in. B & K microphone; □, $\frac{1}{2}$ in. B & K microphone.

LC-70 and LD-107 transducers respectively. Because the spatial sensitivity of real transducers falls off more slowly than an ideal transducer, the real transducers have a much smaller second peak in the wave-number response, so that the fit of the data to equation (6.3) is poor beyond the first zero of (6.3). However, it was established by numerical calculation that the response beyond the first zero gave a negligible contribution in the present computations for $\Phi_p(\omega)$, so that equation (6.3) and an effective radius were used in the computations, rather than the true wave-number response for each transducer. While this procedure was considered to be sufficiently accurate in the present case, in general the true response should be used, particularly in cases where the contribution at high wave-numbers is significant.

The computed values of $\Phi_p(\omega)/\Phi(\omega)$ are compared with the measured values of $\Phi_m(\omega)/\Phi(\omega)$ in figure 19.

The agreement in the case of the two condenser microphones is good, especially as the errors in the computed values are of opposite sign in the two cases. The agreement for the piezo-electric transducer is poor (in fact the results lie below those of the nominally large $\frac{1}{4}$ in. condenser microphone) in spite of the fact that the frequency response of the transducer to sound pressure fluctuations was measured experimentally before the spectrum measurements. The diaphragm of this transducer consists of a piece of 'Mylar' sheet, 0·001 in. (0·025 mm) thick, cemented to the transducer element and to the surrounding surface. It seems likely that the large effective radius of the transducer was due to incomplete adhesion of the outer part of this diaphragm. There is also some doubt that the sensitivity function used was a good approximation for the piezo-electric transducer.

For the more reliable condenser microphone, figure 19 also shows an attempt to compare the results with the empirical correction of Corcos (1963). This correction assumes that the filtered spatial correlation, $S_{pp}(\mathbf{r}, \omega)$ is given by

$$S_{pp}(\mathbf{r}, \omega) = \phi(\omega) A(\omega\xi/U_c) B(\omega\zeta/U_c) e^{-i\omega\xi/U_c}, \tag{8.3}$$

where A and B are monotonically decreasing functions of their arguments, taken from the experimental results of Willmarth & Wooldridge (1962). U_c is a convection velocity which varies with frequency. The estimated spectrum is then given by

$$\frac{\Phi_p(\omega)}{\Phi(\omega)} = \int \Theta(\boldsymbol{\epsilon}) A(\omega\xi/U_c) B(\omega\zeta/U_c) e^{-i\omega\xi/U_c} d\boldsymbol{\epsilon}, \tag{8.4}$$

where $\Theta(\boldsymbol{\epsilon})$ is the convolution integral of the spatial sensitivity function with itself,

$$\Theta(\boldsymbol{\epsilon}) = \int K(\mathbf{s}) K(\mathbf{s}+\boldsymbol{\epsilon}) d\mathbf{s}. \tag{8.5}$$

The correction shown in figure 19 was computed from the tabulated values of the correction given in Corcos (1963). The agreement with the measured spectra is good for the $\frac{1}{2}$ in. microphone, but rather poor for the $\frac{1}{4}$ in. microphone.

Inspection of the two forms for transducer correction (8.2) and (8.4) shows that they are closely related through a Fourier transform relationship, and that the main difference between them lies in the form assumed for $S_{pp}(\zeta, \omega)$. Corcos assumes that

$$S_{pp}(\mathbf{r}, \omega) = \Phi(\omega) B(\omega\zeta/U_c) A'(\omega\xi/U_c) \tag{8.6}$$

based on the measurements of Willmarth & Wooldridge (1962), whereas we have used $\hat{S}_{pp}(\mathbf{k}, \omega) = \hat{S}_{pp}(k_3 U_c/\omega, \omega) F(\omega/k_1 U_c)$, which corresponds to

$$S_{pp}(\mathbf{r}, \omega) = G(\omega\zeta/U_c, \omega) A'(\omega\xi/U_c). \tag{8.7}$$

The use of equation (8.3) as a generally valid form for the wall pressure spectrum has been criticized more recently by Willmarth & Roos (1965), who also used measurements with different sized transducers to show that the correction could not be expressed as a function only of $(\omega R/U_c)$, where R is the transducer radius, as

required by the similarity scaling of Corcos. In general, their measured corrections were smaller than those predicted by Corcos (1963). No direct comparison can be made between the present results and those of Willmarth & Roos, because the transducers used here were much larger than those of the latter authors. However, the two sets of results are consistent in showing a smaller correction than that of Corcos at the higher frequencies. At the highest frequencies, the Corcos type of scaling is expected to hold, because of the wall-similarity considerations discussed by Bradshaw (1967). But, as already noted, the wave-number range in which this is expected to occur corresponds to transducer separations of about the minimum attainable in these experiments. The only prediction of wall-similarity scaling that can be checked is the form of the true frequency spectrum at high frequencies. The orifice probe is sufficiently small to resolve the small scale motion without error up to about 6 kHz, so it should be possible to detect part of the region of wall similarity, which is expected to be centred on a frequency of about 4 kHz. Dimensional arguments lead us to expect the wave-number spectrum in this region to fall like k_1^{-1}, since k_1 is the only relevant length parameter, and by the same argument the frequency spectrum should fall like ω^{-1}. The extent of the ω^{-1} variation is determined by the requirement that the eddies have scales comparable with the spatial limits of the wall-similarity region, giving a lower limit of $\omega\delta^*/U_\infty = 0{\cdot}6$ and an upper limit of $\omega\nu/U_\tau^2 = 0{\cdot}5$ ($\omega\delta^*/U_\infty = 13$ in this case). Thus at the low-frequency end the spectrum will be dominated by large scale fluctuations from the outer layer, and at the high-frequency end by the highly-damped sublayer fluctuations. This is clearly shown by Hodgson's results (figure 17), but not by those taken with the 0·036 in. (0·91 mm) orifice probe, which was too large to resolve the sublayer contribution. Even so, there is an appreciable region for both transducers having a slope of about $-0{\cdot}8$. It is not clear why the slope is significantly less than the predicted -1; earlier suggestions (Bradshaw 1967) that the frequency spectrum should have a lower slope than the wave-number spectrum because of the variation of local convection velocity across the layer are thought to be incorrect because U_c appears in both the abscissa and the ordinate of the frequency spectrum and maintains the slope at -1.

9. Conclusions

Most of the extraneous contribution to the frequency spectrum at low frequencies in low-speed wind tunnel measurements of pressure fluctuations appears to arise in the wind-tunnel diffuser and to travel upstream as acoustic waves. For such experiments, a blower tunnel whose working section exhausts directly into a large volume is to be preferred. Where this is impracticable, the $(\mathbf{k}, c)$ spectrum approach allows the acoustic contribution to be separated from the turbulence contribution.

In a zero-pressure-gradient boundary layer, the upstream-travelling energy, apart from any acoustic component, appears to be negligible in comparison with the downstream-travelling energy at any wave-number.

The distribution of energy over the phase velocity band is roughly normal at all

wave-numbers, with a standard deviation of 0·14, centred on a peak energy velocity which varies from $0{\cdot}9\,U_\infty$ at low wave-numbers.

The filtered correlations with lateral separation at zero longitudinal separation do not appear to scale on any simple frequency parameter.

A functional form for the pressure field has been proposed (equation (8.1)), based on the experimental results, which appears to predict the frequency spectrum measured with large transducers quite accurately.

The measurements show the importance of allowing for the transducer spatial response in determining spectrum corrections at large wave-numbers where $ka > 1$.

I am indebted to Mr P. Bradshaw for many helpful discussions, to Mr G. K. Knight who carried out the experimental work, and to Mr D. H. Ferriss who programmed the numerical calculations discussed in § 8. The work described has been carried out as part of the Research Programme of the National Physical Laboratory.

REFERENCES

BRADSHAW, P. 1967 *J. Fluid Mech.* **30**, 241.

BRADSHAW, P. & HELLENS, G. E. 1964 *Aero. Res. Counc. R & M* 3437.

BRÜEL, P. V. & RASMUSSEN, G. 1959 *Brüel & Kjaer Technical Review*, 2–1959, 1.

BULL, M. K. & WILLIS, J. L. 1961 *University of Southampton A.A.S.U. Rep.* 199.

CORCOS, G. M. 1962 *University of California. Inst. of Eng. Res. Rep. series* 183, no. 2.

CORCOS, G. M. 1963 *J. Acoust. Soc. Am.* **35**, 192.

FAVRE, A., GAVIGLIO, J. J. & DUMAS, R. 1957 *J. Fluid Mech.* **2**, 313.

FAVRE, A., GAVIGLIO, J. & FOHR, J. P. 1964 *Proc. XIth Int. Congr. Appl. Mech.* 878.

GILCHRIST, R. B. & STRAWDERMAN, W. A. 1965 *J. Acoust. Soc. Am.* **38**, 298.

HARRISON, M. 1958 *David Taylor Model Basin Report* 1260.

JOHNSON, R. F. 1962 *Aero. Res. Counc. Current Paper* 685.

KOVASZNAY, L. S. G. & REMENYIK, C. J. 1962 *Proc.* 1962 *heat transfer and Fluid Mech. Inst.* 76.

KRAICHNAN, R. H. 1956 *J. Acoust. Soc. Am.* **28**, 378.

LANDAHL, M. T. 1967 *J. Fluid Mech.* **29**, 441.

LILLEY, G. M. & HODGSON, T. H. 1960 *AGARD Rep.* 276.

LIN, C. C. 1952 *Quart. Appl. Math.* **10**, 295.

SHARMA, R. 1968 Ph.D. Thesis, Southampton.

UBEROI, M. S. & KOVASZNAY, L. S. G. 1953 *Quart. Appl. Math* **10**, 375.

WILLMARTH, W. W. & ROOS, F. W. 1965 *J. Fluid Mech.* **22**, 81.

WILLMARTH, W. W. & WOOLDRIDGE, C. E. 1962 *J. Fluid Mech.* **14**, 187.

WILLS, J. A. B. 1964 *J. Fluid Mech.* **20**, 417.

WILLS, J. A. B. 1968*a* *J. Sci. Instr. Series* 2, **1**, 447.

WILLS, J. A. B. 1968*b* *J. Acoust. Soc. Am.* **43**, 1049.